JOURNAL OF COMPUTATIONAL PHYSICS 51, 208–226 (1983)

Suprathermal Electron Energy Deposition in Plasmas with the Fokker–Planck Method

B. R. WIENKE

Computing Division, Los Alamos National Laboratory, Los Alamos, New Mexico 87545

Received July 30, 1982; revised November 23, 1982

A one-dimensional, multigroup, discrete-ordinates technique for computing electron energy deposition in plasmas is detailed. The Fokker–Planck collision operator is employed in the continuous approximation and electric fields (considered external) are included in the equation. Bremsstrahlung processes are not treated. Comparisons with analytic and Monte Carlo results are given. Fits to deposition profiles and energy scaling are proposed and discussed for monoenergetic and Maxwellian sources in the range 0–150 keV, with and without uniform fields.

I. INTRODUCTION

The multigroup, discrete-ordinates (S_n) method is well known in neutral particle applications [1–4] but extensions to electron transport require modifications. Primary difficulties are linked to the nonlocal Coulomb interaction and the presence of electromagnetic fields. Mean free paths for Coulomb interactions are small and scattering is highly anisotropic. These two facts strain traditional S_n methods, differencing schemes, and acceleration techniques. Electromagnetic fields redistribute particles in energy and direction and act as anisotropic collision terms. Addition of the Lorentz term $(\mathbf{E} + \mathbf{v} \times \mathbf{B})$ to the electron transport equation necessitates a reworking of numerical algorithms used to solve the equation. These modifications are detailed appropriately in the analysis.

Electron energy deposition calculations in plasmas frequently rely upon Monte Carlo transport techniques [5, 6] in the nondiffusive limit. While Monte Carlo treatments of transport are certainly widespread and well suited to complex geometries, they can be time consuming and costly. For one-dimensional applications the S_n approach is efficient. We have constructed a general purpose electron transport module for one-dimensional applications, ESN [7]., and employ it in this study of suprathermal electrons. At the 2–4% statistical variance level in Monte Carlo calculations, the S_n approach is 50 to 100 times faster, which is no real surprise. Electron transport resembles deep neutral particle penetration since mean free paths are relatively short. Additionally, suprathermal electron energy deposition is a topic of interest in laser fusion studies [8–10]. Transport phenomena have been modeled using both multigroup, flux limited diffusion theory and Monte Carlo

0021-9991/83 $3.00

techniques. A versatile and simpler S_n description is valuable for physical insight, parameter comparisons, and as a computational bridge spanning streaming to diffusive regimes. Within the S_n approach, we parametrize deposition profiles in plasmas and examine energy scaling as a function of distance for monoenergetic and Maxwellian electron sources in the keV range.

II. Fokker–Planck Electron Transport Equation

The steady state electron transport equation with Fokker–Planck collision term [11, 12] and electric fields [7] is written

$$\begin{aligned}\boldsymbol{\Omega}\cdot\nabla f=\gamma_i\frac{Z}{2v^3}\frac{\partial}{\partial\mu}(1-\mu^2)\frac{\partial f}{\partial\mu}+\gamma_e\frac{1}{v^2}\frac{\partial f}{\partial v}\\ +\frac{e}{m_0 v}\mathbf{E}\cdot\nabla_v f+S,\end{aligned}\tag{1}$$

with, as usual, (e/m_0) the electron charge to mass ratio, Z the effective ion charge, f the electron flux, $\mathbf{v}=\boldsymbol{\Omega}v$ the electron velocity, ∇, ∇_v spatial and velocity gradients, $\mathbf{E}$ the electric field, S the external source, and

$$\gamma_{i,e}=4\pi n r_0^2 c^3\ln\Lambda_{i,e},\tag{2}$$

with n the electron number density, r_0 the classical electron radius, and Λ the Coulomb cutoff. The first term on the right-hand side of Eq. (1), called the diffusion term, merely redistributes particle directions, while the second term, called the friction term, slows electrons down. The diffusion term describes electron–ion scattering while the friction term details electron–electron interactions. The third term involving the electric field upscatters and downscatters electrons in energy and also redistributes particle directions, as can be seen from the following reduction. Defining the direction cosine μ in one-dimensional geometries,

$$\mathbf{v}\cdot\mathbf{r}=vr\mu,\tag{3}$$

using the operator identity [13]

$$\nabla_v=\frac{\mathbf{v}}{v}\frac{\partial}{\partial v}+\left(\frac{\mathbf{r}}{vr}+\frac{\mu\mathbf{v}}{v^2}\right)\frac{\partial}{\partial\mu},\tag{4}$$

and taking $\mathbf{E}$ along $\mathbf{r}$, we obtain

$$\left(\frac{e}{m_0 v}\right)\mathbf{E}\cdot\nabla_v f=\left(\frac{e}{m_0 v}\right)\left[\mu E\frac{\partial f}{\partial v}+\frac{E}{v}(1-\mu^2)\frac{\partial f}{\partial\mu}\right].\tag{5}$$

Clearly, the first term on the right-hand side of Eq. (5) slows down or speeds up electrons, depending on the sign of μ, while the second term merely changes particle directions.

In the various geometries, the one-dimensional form of $\boldsymbol{\Omega} \cdot \nabla f$ is

$$\begin{aligned} \boldsymbol{\Omega} \cdot \nabla f &= \mu \frac{\partial f}{\partial x}, && \text{(plane)} \\ &= \frac{\mu}{\rho} \frac{\partial}{\partial \rho} (\rho f) - \frac{1}{\rho} \frac{\partial}{\partial \varphi} (\eta f), && \text{(cylinder)} \\ &= \frac{\mu}{r^2} \frac{\partial}{\partial r} (r^2 f) + \frac{1}{r} \frac{\partial}{\partial \mu} (1 - \mu^2) f, && \text{(sphere)} \end{aligned} \tag{6}$$

for

$$\mu^2 + \eta^2 + \zeta^2 = 1, \qquad \tan \varphi = \frac{\eta}{\mu}. \tag{7}$$

Differencing of all terms, especially the angular part of Eq. (6) which is more complex, should recover the analytic form for divergenceless flow in the infinitesimal limit [1].

The Coulomb cutoff Λ is model dependent to some degree [11]. For electrons, we take the relativistically corrected expression

$$\Lambda_e = 1.22 \times 10^{15} \left(\frac{v}{c}\right) (1 - v^2/c^2)^{-1/2} \, T/n, \tag{8}$$

with T measured in keV and n in cm^{-3}. For ions, we use the Spitzer [14] compilation with tabulates $\ln \Lambda_i$ in the limited ranges

$$10^4 \text{ cm}^{-3} \leqslant n \leqslant 10^{18} \text{ cm}^{-3}, \qquad 50°\text{K} \leqslant T \leqslant 10^6 °\text{K},$$

and the quantum mechanical expression based on the minimum impact parameter above those limits (which is appropriate for our applications)

$$\Lambda_i = 1.30 \times 10^{15} (T/n)^{1/2}) p/m_0), \tag{9}$$

with p and m_0 in KeV. Charge neutrality requires the balance

$$n = \sum_{i=\text{ions}} n_i Z_i, \tag{10}$$

and the ion term in Eq. (1) has been renormalized to the electron density n and effective charge Z through the relationship

$$nZ = \sum_{i=\text{ions}} n_i Z_i^2. \tag{11}$$

The Fokker–Planck collision term is used to describe local charged particle scattering in plasmas. Its derivation is based upon the assumption that the Coulomb cross section peaks in the forward direction and that elastic collisions with small changes in velocity are most probable. Suprathermal electron penetration in plasmas is a representative phenomenon when background temperatures are not high and collective plasma effects are not important. Such is the case in laser irradiated target applications where suprathermal (hot) electrons produced by resonant absorption of intense laser light at a critical density surface propagate through a considerably cooler plasma background of relatively low Z material. At the critical surface, electron densities scale as $(10^{21}/\lambda^2)\,\mathrm{cm}^{-3}$ approximately, with λ the laser wavelength in micrometers. It is thought that the only plasma effect of importance in these laser pellet applications is the localized space-charge separation at the corona sheath of the plasma which produces large electric fields holding the hot electrons in containment. Thus, apart from a boundary field effect, a Fokker–Planck treatment of the suprathermal electrons seems appropriate since the dominant plasma interactions are scattering and slowing down.

We also remark that the particular form of the Fokker–Planck collision term in Eq. (1) is the lower order (in energy tansfer) Boltzmann analog of the full Rosenbluth expression detailed by Killeen and Marx [15]. It is first order in $\partial f/\partial v$ and has been used in S_n applications where straggling (tail effects in computed energy deposition curves) are neglected. References [16–19] and [22] discuss the numerical effects of $\partial^2 f/\partial v^2$ on the solution of the transport equation and [17] obtains the particular Fokker–Planck operator employed herein, but we omit the $\partial^2 f/\partial v^2$ term in the following analysis.

III. Multigroup Discrete Ordinates

The discrete-ordinates approximation assumes that the value of the angular flux, or ordinate, is determined at sets of discrete directions $\Omega_m = (\mu_m, \eta_m, \xi_m)$ with $m = 1, 2, 3, \ldots, M$. The corresponding angular flux is denoted by

$$f_m(\mathbf{r}, \varepsilon) = f(\mathbf{r}, \Omega_m, \varepsilon), \tag{12}$$

with ε the energy. Angular integrals and moments involving f_m are evaluated with quadrature weights w_m

$$\int f(\mathbf{r}, \boldsymbol{\Omega}, \varepsilon)\, d\Omega = 4\pi \sum_{m=1}^{M} w_m f_m. \tag{13}$$

Gaussian sets (μ_m, w_m) are employed in our applications. The angular terms in Eq. (6) are differenced using sets of angular coefficients $\alpha_{m\pm 1/2}$ which satisfy

$$(\alpha_{m+1/2} - \alpha_{m-1/2}) = -k w_m \mu_m, \tag{14}$$

with $k = 0, 1, 2$ in plane, cylindrical, and spherical geometry, respectively, $m \pm \frac{1}{2}$ denoting edge values, and

$$\alpha_{1/2} = \alpha_M = 0. \tag{15}$$

In all geometries, the angular streaming terms are written at the cell center m

$$w_m \left(\frac{\partial f}{\partial \Omega}\right)_m = \alpha_{m+1/2} f_{m+1/2} - \alpha_{m-1/2} f_{m-1/2}, \tag{16}$$

and the recursion relationships, Eq. (14), recover the analytic form in the limit of small mesh spacing [1].

The multigroup approximation consists of a similar partitioning of the energy domain ε into G subintervals, $g = 1, 2, 3, \ldots, G$. The flux for group g is written

$$f_{gm}(\mathbf{r}) = \int_{\varepsilon_g}^{\varepsilon_{g+1}} f_m(\mathbf{r}, \varepsilon)\, d\varepsilon, \tag{17}$$

and represents the total flux in the energy interval. Integrating Eq. (1) over $d\varepsilon$ generates the multigroup equations in the standard fashion [1]. Before writing the S_n equations, we make the diamond approximation [1–3] by assuming that the cell centered angular fluxes are averages of the edge values,

$$2f_{gm} = f_{gm+1/2} + f_{gm-1/2}. \tag{18}$$

Sweeping through the angular mesh recursively requires, by virtue of Eq. (18),

$$f_{gm-1/2} = 2f_{gm-1} - 2f_{gm-2} + \cdots \mp 2f_{g1} \pm f_{g1/2}. \tag{19}$$

The particular term $f_{g1/2}$ corresponds to $\mu = -1$ and is specified to start the calculation in curvilinear one-dimensional geometries.

Integrating Eq. (1) over $d\varepsilon$, making the discrete ordinates approximation and using Eqs. (5), (6), (14), (16), and (18), we obtain for plane, cylindrical, or spherical one-dimensional geometries ($q = x, \rho, r$)

$$\begin{aligned} \mu_m \frac{\partial f_{gm}}{\partial q} + \mu_m \gamma_m q^{-1} f_{gm} &= \gamma_i \frac{Z}{2v_g^3} \frac{\partial}{\partial \mu} (1 - \mu_m^2) \frac{\partial f_{gm}}{\partial \mu} \\ &+ \gamma_e \frac{1}{v_g^2} \frac{\partial f_{gm}}{\partial v} + \frac{e}{m_0 v_g} \left[\mu_m E \frac{\partial f_{gm}}{\partial v} + \frac{E}{v_g} (1 - \mu_m^2) \frac{\partial f_{gm}}{\partial \mu} \right] \\ &+ S_{gm} + \mu_m \gamma_m q^{-1} f_{gm-1/2}, \end{aligned} \tag{20}$$

with v_g the average group velocity and

$$w_m \mu_m \gamma_m = \alpha_{m+1/2} + \alpha_{m-1/2}. \tag{21}$$

Equation (20) is the Fokker Planck transport equation for electrons with electric fields in the S_n representation. All that remains is specific reduction of the derivative terms in Eq. (20).

In the continuous approximation [16, 17] energy transfers (upscatter, downscatter) are only allowed between adjacent groups. The continuous approximation (continuous slowing down) is appropriate for small angle scattering where momentum and energy transfers are small. Such is usually the case for higher-energy, charged particles moving through denser, colder background materials [11, 12]. When collective or large scattering angle processes are important, energy transfers become greater and the scattering matrix must couple more energy groups. The frictional term is thus differenced in the downscatter mode

$$\left(\gamma_e \frac{1}{v_g^2}\right) \frac{\partial f_{gm}}{\partial v} = \left(\gamma_e \frac{1}{v_g^2}\right) \frac{f_{g+1m} - f_{gm}}{\Delta v_g}, \tag{22}$$

while differencing of the field term depends on the sign of μ_m. We write

$$\left(\frac{e\mu_m E}{m_0 v_g}\right) \frac{\partial f_{gm}}{\partial v} = \pm \left[\frac{e\mu_m E}{m_o v_g}\right] \frac{f_{g\pm 1m} - f_{gm}}{\Delta v_g}, \tag{23}$$

where $\pm$ is used as the sign of μ_m. The angular derivatives are cast into the form of an "inscatter minus outscatter" source by expanding the angular flux in spherical harmonics. Details are recounted elsewhere [16, 17] and we quote the final result

$$\gamma_t \left(\frac{Z}{2v_g^3}\right) \frac{\partial}{\partial \mu} (1 - \mu_m^2) \frac{\partial f_{gm}}{\partial \mu} = \sum_{l=0}^{M-1} \alpha_g^l f_g^l P_l(\mu_m) - \alpha_g^0 f_{gm}, \tag{24}$$

$$\frac{eE}{m_o v_g^2} (1 - \mu_m^2) \frac{\partial f_{gm}}{\partial \mu} = \sum_{l=0}^{M-1} \beta_g^l f_g^l P_l(\mu_m) - \beta_g^0 f_{gm}, \tag{25}$$

with

$$\begin{aligned} \alpha_g^l &= \alpha_g^0 - \alpha_t \left(\frac{Z}{2v_g^3}\right) (l(l+1), \\ \alpha_g^0 &= \alpha_t \left(\frac{Z}{2v_g^3}\right) M(M-1), \end{aligned} \tag{26}$$

and

$$\begin{aligned} \beta_g^l &= \beta_g^0 - \left(\frac{eE}{m_o v_g^2}\right) \frac{2(2l^2 - 2l - 1)}{(2l+3)(2l-1)}, \\ \beta_g^0 &= \left(\frac{eE}{m_0 v_g^2}\right) \frac{2(2M^2 - 2M - 1)}{(2M+1)(2M-3)}, \end{aligned} \tag{27}$$

for

$$f_g^l = \sum_{m=1}^{M} w_m f_{gm} P_l(\mu_m). \tag{28}$$

The solution strategy for Eq. (20) is the standard inner–outer iteration scheme [1] employed in production transport codes. The inner sweep is the within group iteration, while the outer sweep is over all energy groups. If upscatter is not present ($\mathbf{E} = 0$), only one outer sweep is necessary since the Fokker–Planck collision term only downscatters particles in energy. The ordering of the groups g is from highest to lowest energy.

Obviously, we recast Eq. (20) into the transport form for spatial differencing

$$\mu_m \frac{\partial f_{gm}}{\partial q} + \mu_m \gamma_m q^{-1} f_{gm} + \sigma_{gm} f_{gm} = Q_{gm}, \tag{29}$$

with

$$\begin{aligned} \sigma_{gm} &= \alpha_g^0 + \beta_g^0 + \gamma_e \frac{1}{v_g^2 \Delta v_g} + \frac{e\mu_m E}{m_0 v_g \Delta v_g}, \\ Q_{gm} &= S_{gm} + \sum_{l=0}^{M-1} (\alpha_g^l + \beta_g^l) f_g^l P_l(\mu_m) + \gamma_e \frac{1}{v_g^2 \Delta v_g} f_{g+1} \\ &\quad + \left(\frac{e\mu_m E}{m_0 v_g \Delta v_g} \right) f_{g\pm 1} + \mu_m \gamma q^{-1} f_{gm-1/2}. \end{aligned} \tag{30}$$

The formal solution to Eq. (29) is

$$\begin{aligned} f_{gm}(q) = f_{gm}^0 &\exp\left[\frac{\sigma_{gm}(q - q_0)}{\mu_m} \right] \left(\frac{q}{q_0} \right)^{-\gamma_m} \\ &+ \exp\left[\frac{-\sigma_{gm} q}{\mu_m} \right] q^{-\gamma_m} \int_{q_0}^{q} dt \exp\left[\frac{\sigma_{gm} t}{\mu_m} \right] \frac{t^{\gamma_m}}{\mu_m} Q_{gm}, \end{aligned} \tag{31}$$

and we retain Eq. (31) exactly in the following. For sake of speed, approximations to the integral are plausible [7] but not of direct importance for this analysis. Any approximation to the integral amounts to a differencing scheme. We have tested a number of schemes based on Eq. (31) and found that the exponential representation is efficient, accurate, and an improvement over lower order approaches. Since electron transport so closely resembles deep neutral particle penetration, an efficient spatial scheme is necessary. Accordingly, we perform the exact numerical integration required by Eq. (31) using an adaptive quadrature technique. [7].

There exist a number of similar analyses for charged particle tracking with the Fokker–Planck operator or an S_n approach. None carry the electric field through the transport equation, but we mention them for completeness. The multigroup diffusion

method of Corman *et al.* [18] is not suitable for localized sources or highly anisotropic scattering. The moments technique of Haldy and Ligou [19] is best in infinite media applications. The LSN method of Antal and Lee [20] and the integral tracking technique of Moses [21] account for frictional energy losses due to scattering but neglect angular deflections. Mehlhorn and Duderstadt [22] modified the TIMEX code to perform electron transport calculations in one-dimensional geometries while Morel [16] showed how to use standard S_n codes to obtain angle-energy integrated quantities for charged particles. The latter two efforts somewhat parallel our developments.

IV. Electron Energy Deposition

Theoretical deposition calculations [23–25] for incident beams of electrons typically use the Spencer moment technique [26] or some close variant. Experimental measurements [27–30] have also been made, as well as (earlier mentioned) detailed Monte Carlo simulations. None of the computational approaches include or consider electromagnetic effects. Some include Bremsstrahlung production. Our intent is to give a rather broad, yet simple, parametrization to energy deposition profiles with and without electric fields, to examine energy scaling of the profiles, and to compare our computations with other analyses for monoenergetic and Maxwellian sources. Bremsstrahlung processes are not included in our development, but extensions to include these processes are feasible within the present framework (as additional scattering terms). In high Z materials and dense, hot backgrounds Bremsstrahlung effects on electron ranges and deposition profiles are nonnegligible. Our Monte Carlo calculations indicate that neglect of electron–ion Bremsstrahlung in the following applications has small effect on results. Since inclusion of Bremsstrahlung production provides another energy loss path for electrons, one reasonably expects some shortening of ranges and sharpening of deposition profiles.

In the context of the previous sections, the local energy deposition is given as the difference between energy inflow and outflow over a spatial mesh cell. Defining local deposition as D, we have

$$D(x_i) = \sum_{g=1}^{G} \varepsilon_g \sum_{m=1}^{M/2} \left[f_{gm}(x_{i+1/2}) A_{i+1/2} - f_{gm}(x_{i-1/2}) A_{i-1/2} \right] w_m |\mu_m| + \sum_{g=1}^{G} \varepsilon_g \sum_{m=M/2}^{M} \left[f_m(x_{i-1/2}) A_{i-1/2} - f_{gm}(x_{i+1/2}) A_{i+1/2} \right] w_m |\mu_m|, \quad (32)$$

with A the appropriate area elements at the spatial cell edges. Leftward directions correspond to $\mu_m \leqslant 0$ $(m = 1,..., M/2)$ while rightward directions correspond to $\mu_m \geqslant 0$ $(m = M/2,..., M)$.

Our first task will be the validation of the transport scheme described in the foregoing. We have made a number of tests and comparisons with exact analytic and

TABLE I

Transmitted Currents for Anisotropic Boundary Source

d (cm)	σ (cm)	j (Exact)	J (Discrete ordinates)
0.5	0.10	0.930	0.930
1.0	0.10	0.869	0.867
1.5	0.10	0.816	0.813
2.0	0.10	0.769	0.765
0.5	1.00	0.571	0.571
1.0	1.00	0.400	0.399
1.5	1.00	0.307	0.305
2.0	1.00	0.250	0.248
0.5	10.00	0.118	0.118
4.0	10.00	0.025	0.025
8.0	10.00	0.008	0.008
10.0	10.00	0.007	0.006

Monte Carlo predictions for a number of different source configurations, geometries, and materials and found good agreement. Consider the following comparisons.

As a simple test of scattering, we take a uniform slab of thickness d and work in the isotropic limit of no slowing down and no fields ($E = \gamma_e = \beta_g = 0$). An anisotropic boundary source of electrons of the form $a + b\gamma$, with γ the angle incidence, is placed on the left boundary. Bethe [31] has analyzed this problem analytically and we compare transmitted currents at the right boundary in Table I. An S_8, single group quadrature, and constant cross section are assigned to the slab. The agreement in the transmitted electron currents is excellent.

Similarly, we treat a highly (forward peaked) anisotropic boundary source of electrons incident upon the same slab of thickness d. We employ an S_6, P_5 corrected cross section expansion [32] in the discrete-ordinates calculation. The cross section is again normalized to unity and slowing down and fields are suppressed. Comparisons of discrete ordinates vs Monte Carlo predictions [5] of the inverse transmitted current at the right boundary are depicted in Fig. 1 for the two boundary source $b\gamma^2$, $b\gamma^5$. The straight line joins the circled discrete-ordinates predictions and the squares give the Monte Carlo results. Agreement is again good.

As a third case, we consider monoenergetic electrons normally incident upon a slab of CH_2 ($d = 0.1342$ cm) with energies of 40, 60, 80, and 100 keV. An S_8, P_7 quadrature with 40, 60, 80, and 100 energy groups is employed. Our energy groups are equally spaced at 1 keV. Figure 2 compares deposition in the slab for each of the four incident energies. The S_n predictions are given by dashed lines and the Monte Carlo [5] results by dots. The agreement is again good and we will shortly consider a parametric representation of the curves.

Finally, consider the monoenergetic electron sources in an H_2 sphere ($d = 0.10$ cm) in the presence of a constant electric field ($E = 2750$ statcoul/cm^2) directed inward

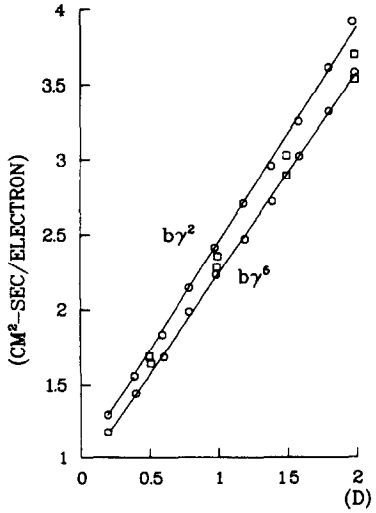

FIG. 1. Inverse transmitted current for anisotropic sources.

along the radius. The field traps the electrons in a smaller effective region, enhances the energy deposition and helps to prevent leakage. Field reversal has the opposite effect. The S_8 results are tabulated with crosses while the Monte Carlo predictions are joined by lines in Fig. 3.

The S_n computations were performed on a spatial mesh of cell width 0.0002 cm. Refining the spatial mesh beyond 0.001 cm resulted in less than 1% change in computed quantities. Typically S_4 angular quadratures were sufficiently accurate to track suprathermal electrons in our applications (3%–6% agreement with Monte Carlo) but we employed S_6 and S_8 sets to further narrow combined spatial-angular

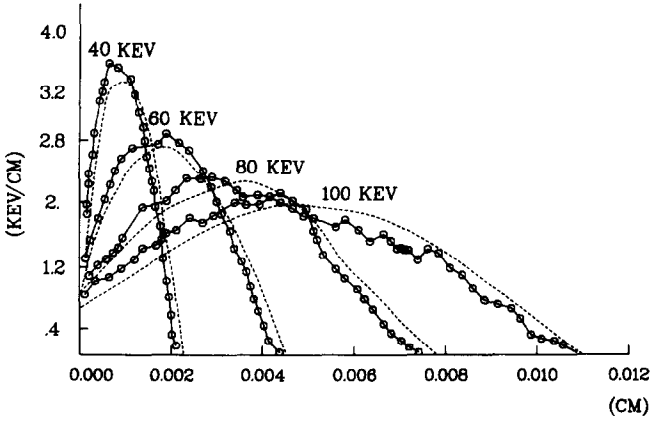

FIG. 2. Deposition profiles in CH_2 for monoenergetic electrons.

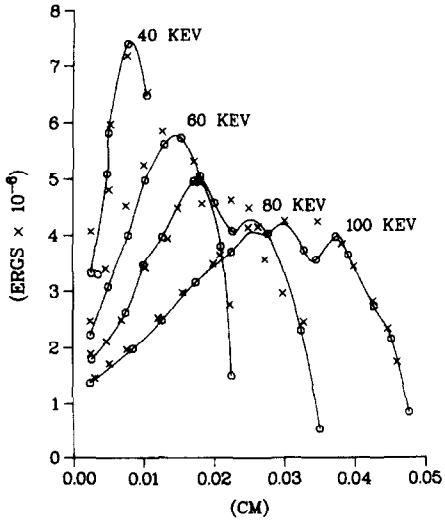

FIG. 3. Deposition profiles in H_2 for monoenergetic electrons in the presence of an electric field.

differencing effects on the solutions. Our cross section expansions were truncated at P_{n-1} for a given S_n order and were transport corrected, thus yielding solution equivalence with the P_{n-1} flux moments expansion results [16, 32].

Close relative agreement in the various comparisons would seem to validate the overall approach. The S_n calculations require seconds while corresponding Monte Carlo computations typically require minutes. As the material regions deepen, the Monte Carlo calculations require more time or become less meaningful statistically.

V. Monoenergetic Electrons, Scaling and Fits

Consider monoenergetic, normally incident beams of electrons on slabs of CH_2, H_2, and LiH plasmas at normal solid density and various background temperatures ($T_e = T_i = 0.333$ keV, 1 keV, 3 keV). A set of deposition profiles for CH_2 at 1 keV has been given in Fig. 2 using an S_8, P_7 multigroup structure. Employing Eq. (32), it is simple to obtain the ranges of electrons in an S_8 calculation of energy deposition. Figure 4 tabulates the corresponding ranges for the three materials at a temperature of $T = 1$ keV for 40, 80, and 120 keV incident electrons. Assuming scaling with energy permits the single parameter power law,

$$R = R_0(\varepsilon/\varepsilon_0)^q, \tag{33}$$

which is least squares fit to Fig. 4 using

$$\ln R = \ln R_0 + q \ln(\varepsilon/\varepsilon_0). \tag{34}$$

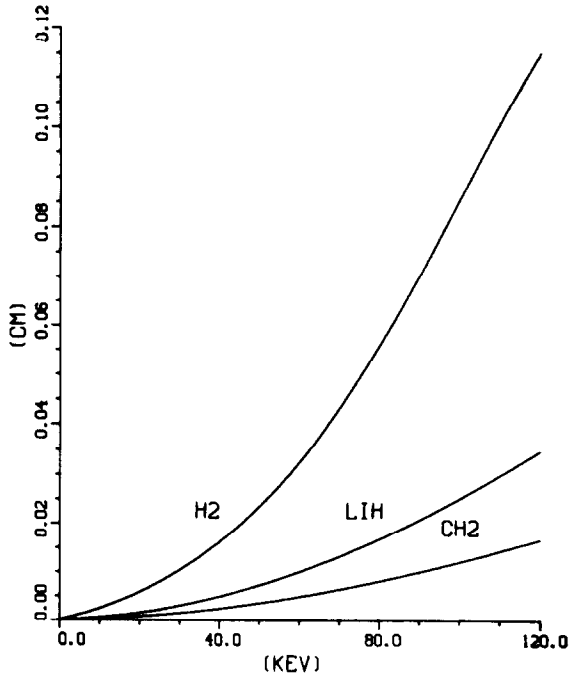

FIG. 4. Range-energy curves in H_2, CH_2, and LiH.

The distance R was obtained from Eq. (32) by requiring $D(R) \leqslant 10^{-4}$ keV. Table II compiles q for the three materials of the various background temperatures. In the range $0 \leqslant \varepsilon \leqslant 150$ keV, we will employ $q = 1.8$. The baselines (ε_0, R_0) can be taken from Table III which lists the range of 100 keV electrons $(\varepsilon_{100}, R_{100})$.

The parabolic shape of the energy deposition profiles, of which Fig. 3 is a representative candidate for CH_2, suggests the fit

$$\frac{\partial D}{\partial x} = a + bx + cx^2, \tag{35}$$

TABLE II

Scaling Fitting Parameter (q)

T (keV)	LiH	CH_2	H_2
0.333	1.813	1.807	1.811
1.000	1.816	1.808	1.813
3.000	1.817	1.809	1.814

TABLE III

Range (R_{100}) of 100 keV Electrons

T (keV)	LiH (cm)	CH_2 (cm)	H_2(cm)
0.333	0.026	0.013	0.092
1.000	0.025	0.012	0.083
3.000	0.024	0.011	0.077

subject to the constraint

$$\int_0^R \frac{\partial D}{\partial x}\, dx = \varepsilon, \tag{36}$$

$$\left.\frac{\partial D}{\partial x}\right|_{x=0} = \frac{4\pi n e^4}{\varepsilon} \ln \Lambda_e, \tag{37}$$

$$\left.\frac{\partial D}{\partial x}\right|_{x=R} = 0, \tag{38}$$

with R the range for incident electron energy ε. Constraint equations (36)–(38) merely enforce energy conservation across the region $0 \leqslant x \leqslant R$ and normalize the initial stopping power to the incident energy [11, 14]. From the above, we find

$$\begin{aligned} a &= \frac{4\pi n e^4}{\varepsilon} \ln \Lambda_e, \\ b &= \frac{2}{R}\left(\frac{3\varepsilon}{R} - 2a\right), \\ c &= \frac{3}{R^2}\left(a - \frac{2\varepsilon}{R}\right). \end{aligned} \tag{39}$$

In these calculations, some of the incident electrons are backscattered out of the medium so that the energy deposited is less than ε. For low Z plasmas, this effect is negligible. For higher Z material, this could be corrected by reduction of the factor ε in Eq. (39). The backscattered leakage is easily computed at the incident boundary.

VI. Maxwellian Electrons, Scaling and Fits

Of particular interest in hot electron applications [9, 10] is the one-dimensional Maxwellian distribution

$$f(\varepsilon) = (\pi T \varepsilon)^{-1/2} \exp(-\varepsilon/T), \tag{40}$$

normalized to unity over $0 \leqslant \varepsilon \leqslant \infty$ for T the temperature. The average energy $\bar{\varepsilon}$ of this distribution is

$$\bar{\varepsilon} = \int_0^\infty \varepsilon f(\varepsilon)\, d\varepsilon = T/2. \tag{41}$$

The energy deposited by a normally incident Maxwellian source of electrons is obtained from Eqs. (35), (39), and (40)

$$\frac{\partial \bar{D}}{\partial x} = (\pi T)^{1/2} \int_{\varepsilon(x)}^\infty \varepsilon^{-1/2}(a + bx + cx^2) \exp(-\varepsilon/T)\, d\varepsilon, \tag{42}$$

with $\varepsilon(x)$ the minimum energy necessary to reach x. To close Eqs. (35) and (42) within the scaling imposed by Eq. (33), elimination of the stopping power term

$$a = \frac{4\pi n e^4}{\varepsilon} \ln \Lambda_e \tag{43}$$

is proposed by the range-energy constraint. In the absence of scattering [11] and by simple dimensional arguments

$$a \sim \varepsilon/R, \tag{44}$$

which, from Eq. (33), yields

$$\frac{\partial \varepsilon}{\partial R} = \frac{\varepsilon}{1.8R} = a. \tag{45}$$

Equation (42) is thus written

$$\frac{\partial \bar{D}}{\partial x} = (\pi T)^{-1/2} \int_{\varepsilon(x)}^\infty \frac{\varepsilon^{1/2}}{1.8R} \exp(-\varepsilon/T)[1 + 6.8(x/R) - 7.8(x/R)^2]\, d\varepsilon. \tag{46}$$

To give some feeling for the goodness of fit, Fig. 5 compares Eq. (46) with an S_{16}, 50 group calculation in CH_2 for $T = 50$ keV. Background temperature in the CH_2 slab was taken to be 1 keV. Agreement between the S_n calculation (dashed line) and the fit equation (46) (solid line) is seen to be excellent for deeper regions and good for shallower penetrations. In the multigroup calculation, we require $0 \leqslant \varepsilon \leqslant 150$ keV as the range consistent with Fig. 4. Above 150 keV, the scaling parameter $q = 1.8$ drops off. Our calculations indicate that a fixed power scaling law, such as Eq. (33), is valid over roughly 150 keV energy ranges and thus the approach described need only be recalibrated to a different scaling parameter q for some other range.

Consistent with Eq. (41),

$$\int_0^\infty \frac{\partial \bar{D}}{\partial x}\, dx = T/2. \tag{47}$$

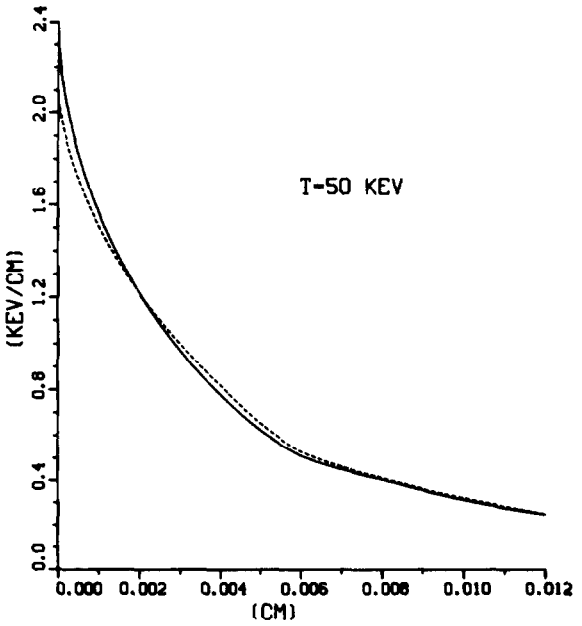

FIG. 5. Deposition profile in CH_2 for Maxwellian electrons.

Changing variables from ε to y,

$$y = x/R, \tag{48}$$

and imposing the scaling law, Eq. (33), so that the lower limit on the integrand of Eq. (46) becomes

$$\varepsilon(x) = \varepsilon_0(x/R_0)^{1/1.8} = (x/\xi)^{1/1.8}, \tag{49}$$

recasts Eq. (4)

$$\frac{\partial \bar{D}}{\partial x} = \kappa \int_0^1 \exp(-\lambda/y^{1/1.8})\, y^{-5/6}(1 + 6.8y - 7.8y^2)\, dy, \tag{50}$$

where

$$\begin{aligned} \kappa &= (1.8)^{-2}\, \pi^{-1/2}(T/\rho)(\rho/\chi)^{1/6}, \\ \lambda &= (x/\rho)^{1/1.8}, \\ \rho &= \xi T^{1.8}. \end{aligned} \tag{51}$$

Employing the asymptotic limits ($\lambda \to 0, \infty$), we fit the deposition profile

$$\frac{\partial \bar{D}}{\partial x} = \kappa \exp(-\lambda)\, G(\lambda), \tag{52}$$

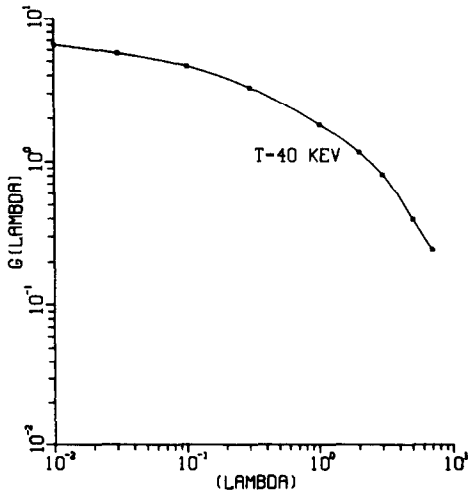

FIG. 6. Fit comparison for maxwellian electrons in H_2.

with

$$G(\lambda) = 8.28(1 + 1.3\lambda^{1/3} + 2.12\lambda + 0.28\lambda^2)^{-1}. \tag{53}$$

Figure 6 compares the fit equation (52) against the exact equation (46) for Maxwellian hot electrons ($T = 40$ keV) incident on a slab of H_2 plasma. The joined line represents the fit while the dots are the result of numerical integration of Eq. (46).

The scaling described in this and the previous section is appropriate for slab geometries. It is not valid in curvilinear geometries unless the range is small compared with the deposition radius or the curvilinear terms in the transport equation (29) are small ($\rho, r \to \infty$). The scaling laws are limited to roughly a range of energy $0 \leqslant \varepsilon \leqslant 150$ keV. At higher energies, $q = 1.8$ underestimates the energy loss in the shallower regions and overestimates energy deposition at greater depths. Extension of the method to higher energies merely requires a recalibration of the power scaling parameter q. In the range $150\text{ keV} \leqslant \varepsilon \leqslant 300\text{ keV}$, for instance, we have found $q = 1.4$.

VII. Electric Fields, Scaling and Fits

The presence of an electric field **E** in the interior of a plasma obviously modifies the deposition and density profile of electrons. Space charge separation produces local fields which self-consistently change electron densities, mean free paths, and hence solutions to the transport equation. In laser pellet applications, for instance, intense electric fields in the plasma sheath surrounding the ablating pellet effectively trap and turn (reflect) leaking electrons back into the target. Equation (29) can be

used easily in general applications involving electric fields where **E** is user specified. However, to quantify field effects on deposition profiles in a manner akin to the previous two sections, we limit discussion to uniform, constant fields in the plasma interior. We also work in the weak field approximation

$$eE \leqslant \frac{4\pi ne^4}{\varepsilon} \ln \Lambda_e, \tag{54}$$

so that the plasma is still collisionally dominated.

From Fig. 3, it is appararent that electric fields increase/decrease effective ranges, but have small effect on the shape of the deposition curve. Taking the constant electric field **E** along the x direction of the slab, we recast Eq. (36)

$$\int_0^R \frac{\partial D}{\partial x}\, dx = \varepsilon \pm eER, \tag{55}$$

where the plus sign holds for electric fields directed in the positive direction and the minus sign for fields in the negative direction. Generally, the plus sign holds for fields in the direction of electron streaming while the minus sign is employed for fields acting against the flow. The boundary normalizations Eq. (37) and (38), remain unchanged. Applying Eqs. (37), (38), and (55) to Eq. (35) yields

$$\begin{aligned} a &= \frac{4\pi ne^4}{\varepsilon} \ln \Lambda_e, \\ b &= \frac{6}{R^2}\left(\varepsilon \pm eER - \frac{aR^3}{3}\right), \\ c &= \frac{6}{R^3}\left(\frac{aR}{2} - \varepsilon \mp eER\right). \end{aligned} \tag{56}$$

Equation (55) merely conserves energy in the system,

$$\int_0^R \mathbf{F} \cdot \mathbf{dx} = \varepsilon + \int_0^R e\mathbf{E} \cdot \mathbf{dx}, \tag{57}$$

with **F** the total force. The previous scaling law, Eq. (33), is rewritten

$$R = R_0 |(\varepsilon \pm eER)/(\varepsilon_0 \pm eER_0|^q, \tag{58}$$

and thus recalibrates the range-energy curves to eE. All the foregoing analyses remain intact with the new definitions implied by Eqs. (56) and (58).

Figure 7 compares the fit equation (56) to the results obtained for 60 keV normally incident electrons in an S_8, P_7 corrected multigroup calculation. Agreement is excellent. The line represents the fit while the dots correspond to the S_8 calculation ($E = 2750$ statcoul/cm^2) in H_2.

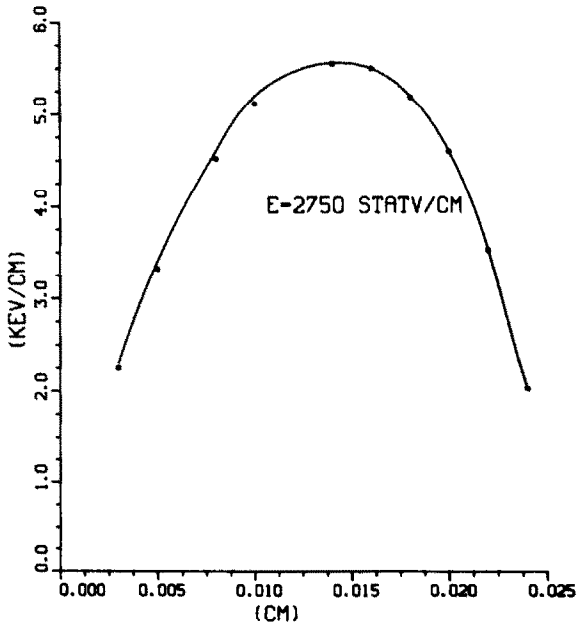

FIG. 7. Deposition profiles and fit comparison for 60 keV electrons in the presence of an electric field.

VIII. Summary

We have detailed the one-dimensional approach, methods, and modifications for transporting electrons in plasmas with the S_n method in the Fokker–Planck approximation. Detailed comparisons and predictions of the method have been given which show that the approach is accurate, efficient, and convenient. Focusing on slab geometry, parametric fits to energy deposition profiles have been obtained using a power scaling law (range-energy curve) valid over a range of 150 keV. Electric fields have been included in the analysis under the weak field limit. As a production technique in large code applications, the S_n method for electrons is a viable alternative to more time-consuming Monte Carlo calculations and a valuable means for parameter and benchmark studies.

ACKNOWLEDGMENTS

We thank R. Alcouffe and T. Hill (LANL) for helpful S_n discussions and J. Mack (LANL) and S. Chavin (MRC) for advice on the Monte Carlo computations.

REFERENCES

1. B. G. CARLSON AND K. D. LATHROP, *in* "Computing Methods in Reactor Physics," Gordon & Breach, New York, 1968.
2. T. R. HILL, "ONETRAN: Discrete Ordinates Finite Element Code for the Solution of the One Dimensional Multigroup Transport Equation," Los Alamos National Laboratory Report LA-5990-MS, June 1975.
3. T. R. HILL AND W. H. REED, "TIMEX: Time Dependent Explicit Discrete Ordinates Program for the Solution of Multigroup Transport Equations With Delayed Neutrons," Los Alamos National Laboratory Report LA-6201-MS, February 1976.
4. B. R. WIENKE, "SNEX: Semianalytic Solution of the One Dimensional Discrete Ordinates (S_n) Transport Equation With Diamond Differenced Angular Fluxes," Los Alamos National Laboratory Report LA-7879-MS, June 1979.
5. J. A. HALBLEIB, SR. AND W. H. VANDEVENDER, "CYLTRAN: A Cylindrical-Geometry Multimaterial Electron/Photon Monte Carlo Transport Code," Sandia Laboratory Report SAND-74-0030, March 1975.
6. M. J. BERGER AND S. M. SELTER, "ETRAN Monte Carlo Code System for Electron and Photon Transport Through Extended Media," Radiation Shielding Information Center Report, CCC-107, June 1968.
7. B. R. WIENKE, *J. Quant. Spectrosc. Radiat. Transfer* **28** (1982), 311; *Nucl. Sci. Eng.* **81** (1982), 302.
8. M. D. ROSEN, D. W. PHILLION, V. C. RUPERT, W. C. MEAD, W. L. KRUER, J. J. THOMPSON, AND H. N. KORNBLUM, *Phys. Fluids* **22** (1979), 2020.
9. P. W. FORSLUND, J. M. KINDEL, K. LEE, E. L. LINDSTROM, AND R. L. MORSE, *Phys. Rev. A* **11** (1975), 679.
10. K. G. ESTABROOK AND W. L. KRUER, *Phys. Rev. Lett.* **40** (1978), 42.
11. I. P. SHKAROFSKY, T. W. JOHNSTON, AND M. P. BACHYNSKI, "Particle Kinetics of Plasmas," Addison–Wesley, Reading, Mass., 1976.
12. D. MOSHER, *Phys. Fluids.* **18** (1975), 846.
13. B. R. WIENKE, *Phys. Fluids* **17** (1974), 1135.
14. L. SPITZER, "Physics of Fully Ionized Gases," Interscience, New York, 1956.
15. J. KILLEEN AND K. D. MARX, "Methods in Computational Physics," Vol. 9, Academic Press, New York, 1970.
16. J. E. MOREL, *Nucl. Sci. Eng.* **79** (1981), 340; *Nucl. Sci. Eng.* **71** (1979), 64.
17. B. R. WIENKE, *Nucl. Sci. Eng.* **79** (1981), 430; *J. Quant. Spectrosc. Radiat. Transfer* **22** (1979), 301; *J. Quant. Spectrosc. Radiat. Transfer* **24** (1980), 385.
18. E. G. CORMAN, W. E. LOEWE, G. E. COOPER, AND A. M. WINSLOW, *Nucl. Fusion* **15** (1975), 377.
19. P. A. HALDY AND J. LIGOU, *Nucl. Fusion* **17** (1977), 1225; *Nucl. Sci. Eng.* **79** (1981), 269.
20. M. J. ANTAL AND C. J. LEE, *J. Comput. Phys.* **20** (1976), 298.
21. G. A. MOSES, *Nucl. Sci. Eng.* **64** (1977), 49.
22. T. A. MEHLHORN AND J. J. DUDERSTADT, *J. Comput. Phys.* **38** (1980), 86.
23. T. TABATA AND R. ITO, *Nucl. Sci. Eng.* **53** (1974), 226.
24. I. ADAWI, *Phys. Rev.* **107** (1957), 1476.
25. R. J. HARRACH AND R. E. KIDDER, *Phys. Rev. A* **23** (1981), 887.
26. L. V. SPENCER, *Phys. Rev.* **98** (1955), 1957.
27. J. R. YOUNG, *J. Appl. Phys.* **28** (1957), 524.
28. Y. NAKAI, Jap. *J. Appl. Phys.* **2** (1963), 743.
29. T. E. EVERHART AND P. H. HOFF, *J. Appl. Phys.* (1971), 5837.
30. S. CHAPPELLE AND J. HUMPHREYS, *IEEE Trans. Nucl. Sci.* **17** (1970), 272.
31. H. A. BETHE, M. E. ROSE, AND L. P. SMITH, *Proc. Amer. Philos. Soc.* (1938), 573.